nature energy

Article

https://doi.org/10.1038/s41560-023-01263-2

Grooved electrodes for high-power-density fuel cells

Received: 22 November 2022

Accepted: 14 April 2023

Published online: 25 May 2023

Check for updates

ChungHyuk Lee[1,2], Wilton J. M. Kort-Kamp[3], Haoran Yu[4], David A. Cullen[4], Brian M. Patterson[5], Tanvir Alam Arman[1], Siddharth Komini Babu[1], Rangachary Mukundan[1,6], Rod L. Borup[1] & Jacob S. Spendelow[1]

Proton exchange membrane fuel cells (PEMFCs) are leading candidates to decarbonize the transport sector, but widespread deployment will require improvements in lifetime, fuel economy and cost. Here we present the grooved electrode, an alternative electrode structure that enhances PEMFC performance and durability by coupling high ionomer (ion-conducting binder) content for improved H^+ transport with grooves for rapid O_2 transport. Grooved electrodes provide up to 50% higher performance than state-of-the-art conventional electrodes under standard operating conditions. Fuel cell diagnostics combined with multiphysics modelling demonstrate that grooved electrodes provide facile O_2 transport despite their high ionomer content, enabling improved reaction rate uniformity. Grooved electrodes also provide improved durability, with less performance loss after carbon corrosion compared with baseline electrodes. Machine learning analysis demonstrates the potential to further optimize grooved structures for next-generation PEMFCs with enhanced performance and durability, enabling smaller and cheaper fuel cell stacks with higher fuel efficiency.

As the global surface temperature continues to rise[1], efforts to replace fossil fuel-based power sources with clean energy alternatives are growing rapidly[2]. Proton exchange membrane fuel cells (PEMFCs) provide an attractive replacement for internal combustion engines in transportation applications due to their ability to produce on-demand electricity with zero local carbon emissions[3–5]. By using renewable H_2 produced by water electrolysis, PEMFCs can eliminate the dependence of the transport sector on fossil fuels. Heavy duty trucking represents a particularly promising opportunity for PEMFCs, because it requires a relatively small number of fuelling stations and also heavy duty vehicles (HDVs) have less stringent capital cost requirements than light duty vehicles. Furthermore, the electrification of HDVs using batteries is relatively difficult due to the need for long range, fast refuelling, low weight and small size, making PEMFCs a leading contender to power zero-emission HDVs. However, improvements in durability[6–8] and efficiency (fuel economy)[9], along with reductions in capital cost, are needed to facilitate commercialization[10]. The development of improved electrode materials is needed[11–20], but the way these materials are arranged and interfaced within the electrode also plays a pivotal role in achieving high power density, durability and efficiency. Increasing power density and thereby reducing stack size is a particularly promising route to capital cost reduction, because reduced material cost is accompanied by the additional benefits of lower volume and weight. Improved electrode design that provides faster transport and more effective use of materials can provide higher power density, durability and efficiency as well as lower capital cost, as demonstrated here.

Conventional PEMFC electrodes are composed of a carbon-supported platinum catalyst (Pt/C) and ionomer, mixed in an ink slurry

[1]Materials Physics and Applications Division, Los Alamos National Laboratory, Los Alamos, NM, USA. [2]Department of Chemical Engineering, Toronto Metropolitan University, Toronto, Ontario, Canada. [3]Theoretical Division, Los Alamos National Laboratory, Los Alamos, NM, USA. [4]Center for Nanophase Materials Sciences, Oak Ridge National Laboratory, Oak Ridge, TN, USA. [5]Materials Science and Technology Division, Los Alamos National Laboratory, Los Alamos, NM, USA. [6]Present address: Energy Technologies Area, Lawrence Berkeley National Laboratory, Berkeley, CA, USA. e-mail: spendelow@lanl.gov

https://doi.org/10.1038/s41560-023-01263-2

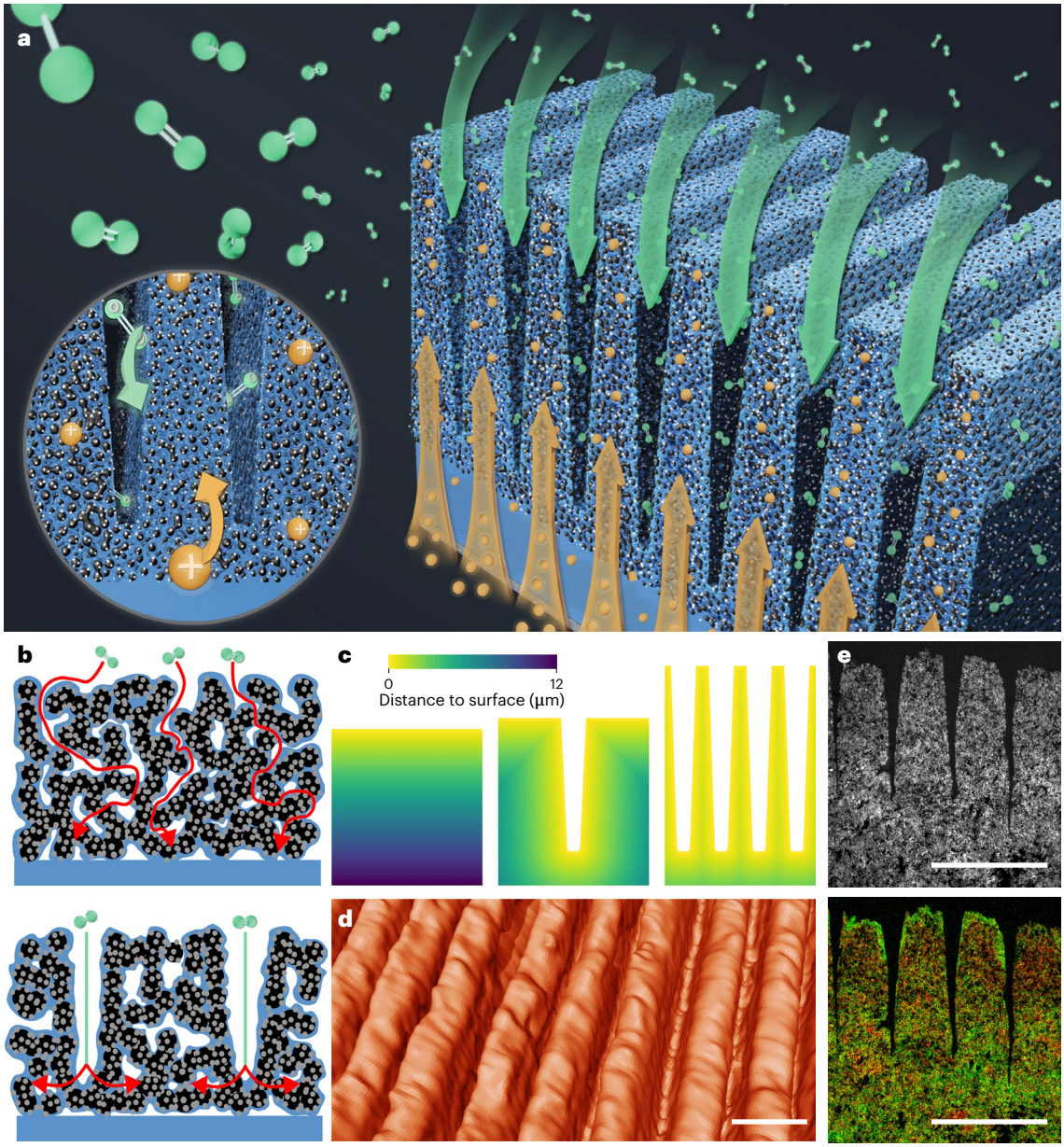

Fig. 1 | Grooved electrode concept. a, Schematic of the working mechanism of grooved electrodes: high-ionomer-content ridges facilitate enhanced transport of H^+ (orange), while grooves provide effective O_2 transport (green), enabling improved fuel cell performance. **b**, Schematics showing O_2 transport through flat (top) and grooved (bottom) electrodes, highlighting the origin of reduced O_2 transport resistance in grooved electrodes. **c**, Euclidean distance from the interior of the electrode to the surface. The average distances to the surface for flat electrodes and grooved electrodes with 12 μm and 3 μm groove spacing are 6.0 μm, 2.5 μm and 0.73 μm, respectively. **d**, Reconstructed nanoscale computed X-ray tomogram of a grooved electrode. **e**, HAADF-STEM image (top) and STEM-EDS elemental map (bottom) of a 1 μm/3 μm (I/C = 1.2) electrode. Red, Pt; green, F. Scale bars, 5 μm.

and deposited on a membrane or gas diffusion layer (GDL) as a porous electrode[21,22]. This top-down process creates a randomized electrode structure with tortuous ionomer and pore networks that limit mass transport and lower catalyst utilization[23–25]. Strikingly, the conventional electrode used in today's commercial PEMFCs is little changed from the structure pioneered by Wilson and Gottesfeld more than 30 years ago[26]. To overcome the limitations of conventional electrode structures, several studies have focused on designing alternative architectures enabled by advances in micro- and nanofabrication techniques[23,27,28], inkjet printing[29,30], template-based patterning[31–33] and thin-film deposition[30,34]. While many of these alternative electrode structures provide improvements in mass activity, transport and/or durability, these advantages tend to manifest under limited operating conditions and have not been demonstrated across the wide range of conditions encountered in transportation applications[23]. Specifically, enhanced performance at relevant voltages (≥0.7 V) and under lower relative humidity conditions is crucial for HDV applications[4].

Here we report the grooved electrode, an alternative electrode design that provides improved performance under a wide range of humidity conditions, with notably improved durability. The architecture of this electrode features two main characteristics: high-ionomer-content electrode ridges that provide facile H^+ transport separated by grooves (void channels) that facilitate O_2 diffusion for the rapid delivery of oxygen reduction reaction (ORR) reactants to the reaction sites (Fig. 1a). In conventional flat electrodes, a high ionomer content can enhance H^+ transport[35], but this enhancement comes with a severe penalty of higher O_2 transport resistance[36]. Therefore, conventional electrode design involves a painful compromise between

https://doi.org/10.1038/s41560-023-01263-2

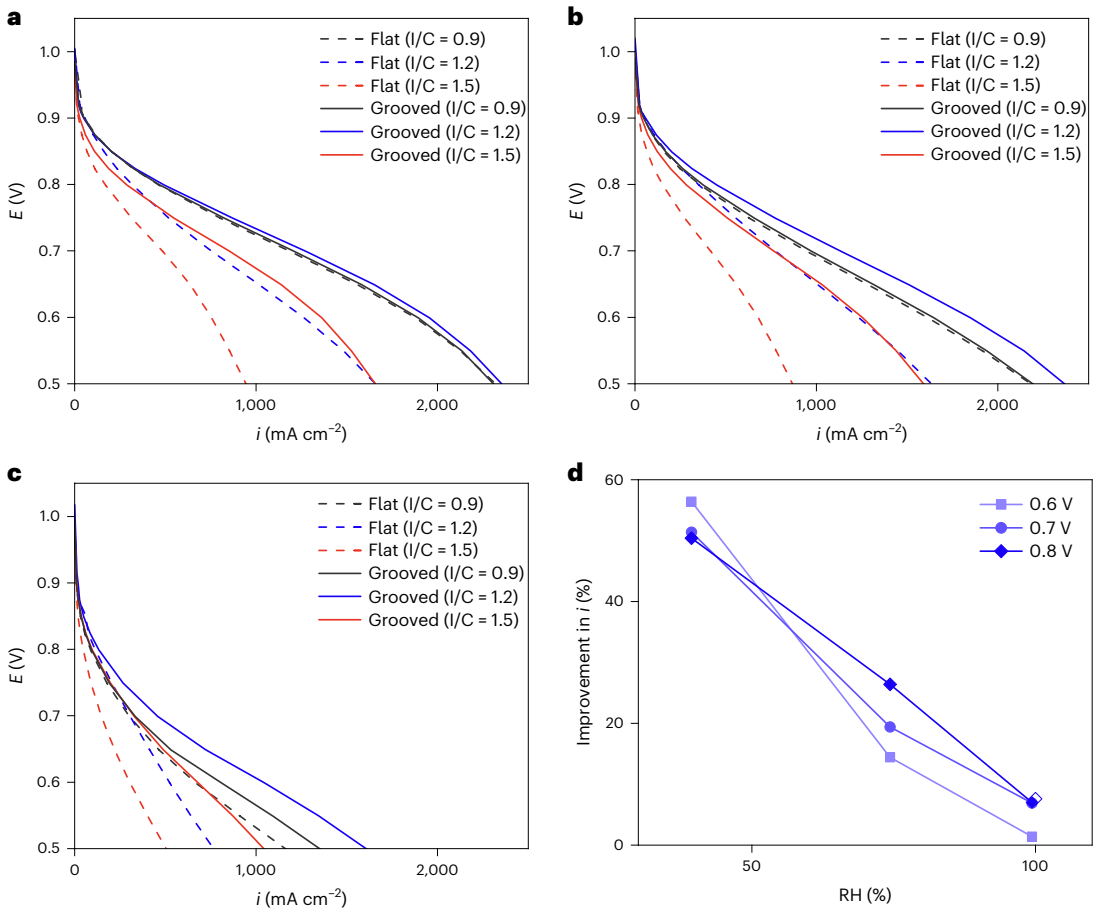

Fig. 2 | Performance of fuel cells with flat and grooved electrodes. a–c, Polarization curves demonstrating the effects of I/C ratio on *i* of flat and grooved electrodes (1 µm/3 µm) at 150 kPa_{abs}, 80 °C, H_2/air and 100% RH (**a**), 75% RH (**b**) and 40% RH (**c**). *E*, applied potential. **d**, Performance enhancement provided by the grooved electrode relative to a flat electrode at their optimal I/C values (1.2 and 0.9, respectively) at different voltages. The cathode loading was 0.3 mg_{Pt} cm^{-2}, with less than 5% variation. The current density was calculated by dividing the measured current by the geometric active area of 5 cm^2.

the conflicting needs of O_2 and H^+ transport. While previous works have reported electrode structures with macropore designs to enhance the transport of a single reactant[37,38], our work presents a multifunctional electrode with highly ordered ridge and groove structures that simultaneously enhance the transport of both H^+ and O_2. By partitioning the transport pathways of O_2 and H^+ into grooves and ridges, respectively, the grooved electrode provides an attractive solution to the problems inherent in conventional electrodes, enabling substantial performance and durability improvements that could enable PEMFC deployment in HDV applications.

Characterizing the grooved electrode morphology

The foundation of the grooved electrode concept lies in the hypothesis that electrode grooves can reduce the effective diffusion length for O_2 transport to ORR reaction sites. Whereas O_2 transport in flat electrodes requires long-distance diffusion through a complex network of narrow and tortuous pores, grooved electrodes provide rapid diffusion through the void space of the grooves, followed by short-distance lateral diffusion into the ridges (Fig. 1b). We quantitatively demonstrated this concept by calculating the Euclidean distance between the interior and surface of the electrode (Fig. 1c). As grooves are added and the spacing between grooves decreases, the average distance to the surface is reduced eightfold relative to the flat electrode (6.0–0.73 µm).

Grooved electrodes were fabricated by depositing a mixture of Pt/C and ionomer on a patterned Si template, followed by transfer to a Nafion membrane. The resulting electrodes exhibited a well-defined groove and ridge structure, verified in three dimensions by nanoscale computed X-ray tomography (Fig. 1d). This method provides a high degree of control of the grooved electrode morphology with a relatively uniform Pt and ionomer distribution, as evidenced by high-angle annular dark-field scanning transmission electron microscopy (HAADF-STEM) and energy-dispersive X-ray spectroscopy (EDS) images of the grooved electrodes (Fig. 1e). The grooved electrodes tested in this study included grooves with dimensions of 2 µm/6 µm, 1.5 µm/4 µm and 1 µm/3 µm, where the first and second numbers represent the groove width (top) and period, respectively, as measured from the top views of their scanning electron microscopy (SEM) images (Supplementary Fig. 1). Both the groove width and groove spacing were reduced to maintain a similar electrode thickness, and the grooves were oriented perpendicular to the flow channels.

Grooved electrodes enhance fuel cell performance

The performance (*i*) of flat and grooved electrodes based on commercial TEC10E40E Pt/C with a range of ionomer-to-carbon (I/C) ratios is shown in Fig. 2a–c. Higher ionomer content leads to smaller electrode pores with higher tortuosity[39], causing severe O_2 transport limitations due to lower Knudsen diffusivity[40] and longer diffusion length. Slow O_2 diffusion through ionomer films further contributes to the high O_2 transport resistance[41,42]. As a result, the flat electrodes exhibited decreasing performance as the I/C ratio increased above the optimal

https://doi.org/10.1038/s41560-023-01263-2

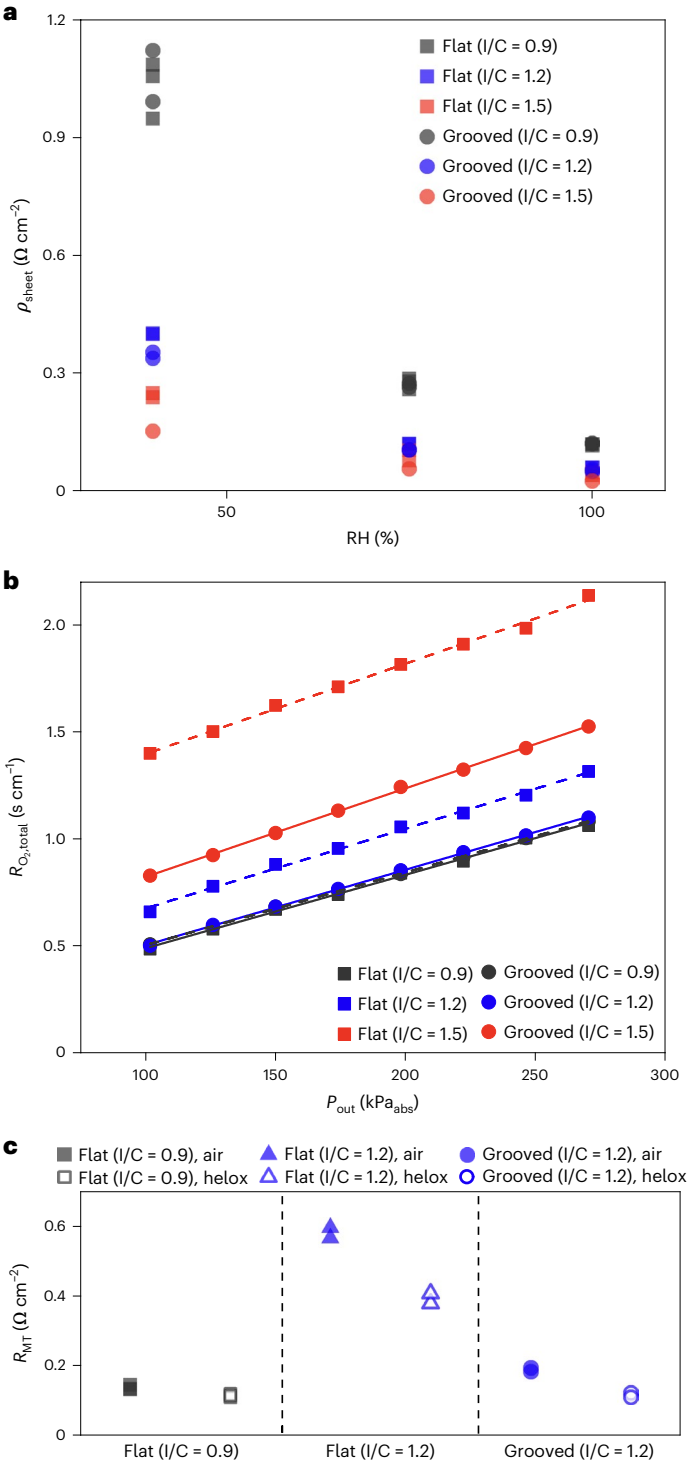

Fig. 3 | Transport resistance in flat and grooved (1 µm/3 µm) electrodes. **a**–**c**, Sheet resistance (**a**), O_2 transport resistance measured at 60% RH (R_{O2},total, the combined pressure-dependent and pressure-independent transport resistance; P_{out}, the outlet pressure in kPa$_{abs}$) (**b**) and R_{MT} measured at 100% RH (**c**). Multiple markers in **a** and **c** represent data from repeated measurements. The equivalent circuit models are shown in Supplementary Figs. 3 and 4, parameters are shown in Supplementary Tables 1 and 2, and linear regression results are shown in Supplementary Table 3.

value of 0.9 (ref. 36). In contrast, the grooved electrodes exhibited peak performance for an I/C ratio of 1.2, showing a higher performance than the optimized flat electrode (I/C = 0.9) across a wide range of relevant operating conditions (Fig. 2d), due to the combination of rapid O_2 transport through the grooves and rapid H^+ transport through the high I/C ridges. The grooves provided greater improvements under low relative humidity (RH) conditions, when both O_2 and H^+ transport become limiting due to the dehydration of the ionomer. Low RH operation is important for vehicle applications, where humidification is limited and a high cell temperature is needed for effective heat rejection[4]. In addition, a higher performance at low RH enables robust and consistent power generation across a broad range of humidity. For instance, when the humidity was decreased from 100% to 75% RH, the flat electrode (I/C = 0.9) performance decreased by 20% at 0.7 V (1.19 to 0.95 A cm^{-2}, 0.83 to 0.66 W cm^{-2}), whereas the grooved electrode (I/C = 1.2) performance decreased by only 11% (1.28 to 1.14 A cm^{-2}, 0.90 to 0.80 W cm^{-2}). Cell performance increased with decreasing groove period (Supplementary Fig. 2), further confirming the important role of grooves in providing short effective O_2 diffusion lengths. These results demonstrate the compelling benefits of the grooved electrode design for enhanced PEMFC performance.

Grooved electrodes lower H^+ and O_2 transport resistance

The O_2 and H^+ transport resistance was measured using limiting current methods and electrochemical impedance spectroscopy (EIS; Fig. 3). As the I/C ratio increased, the sheet resistance (ρ_{sheet}, a measure of H^+ transport resistance in the cathode electrode, measured by EIS in H_2/N_2 (ref. 43)) decreased notably, regardless of the presence of grooves (Fig. 3a).

While the use of higher I/C reduces the sheet resistance, it also results in smaller pores and thicker ionomer films, impeding O_2 transport. Indeed, limiting current measurements[44] in 0.5% O_2 revealed a significant increase in O_2 transport resistance (R_{O_2}) with increasing I/C in flat electrodes (as indicated by the dashed lines in Fig. 3b). The pressure-independent R_{O_2} (that is, the *y* intercept) was 96% and 530% higher for I/C = 1.2 and 1.5, respectively, relative to I/C = 0.9. This extreme increase in R_{O_2} confirms that the lower performance observed with high I/C flat electrodes is a result of the slower O_2 transport at higher I/C. Notably, the incorporation of grooves into electrodes caused a more than 50% reduction in the pressure-independent R_{O_2} for I/C = 1.2 and 1.5. The R_{O_2} values for the flat (I/C = 0.9) and grooved (I/C = 1.2) electrodes are nearly identical, demonstrating that grooves provide facile O_2 transport even in high I/C electrodes.

While the limiting current methods provided valuable information about O_2 transport, the measurements were performed under conditions quite different from normal cell operation. Therefore, we used EIS to determine the O_2 mass transport resistance (R_{MT})[45] in air and helox (79% He, 21% O_2; Fig. 3c). R_{MT} in air describes both pressure-dependent and -independent resistance, whereas R_{MT} in helox predominantly describes pressure-independent resistance, because the O_2 diffusion coefficient in He is around four times larger than that in N_2 (ref. 46). In flat electrodes, an increase in I/C from 0.9 to 1.2 caused a 430% and 350% increase in R_{MT} in air and helox, respectively. However, the incorporation of grooves into electrodes with I/C = 1.2 led to a 66% and 68% decrease in R_{MT} in air and helox, respectively. At the optimized I/C values of 0.9 (flat) and 1.2 (grooved), the electrodes showed nearly identical R_{MT} in helox, confirming that grooves enable effective pressure-independent O_2 diffusion even at high I/C. Overall, the grooved electrode with I/C = 1.2 provided rapid O_2 diffusion similar to the flat I/C = 0.9 electrode, while simultaneously providing rapid H^+ transport similar to the flat I/C = 1.2 electrode. Grooves have a negligible effect on the electrochemical surface area (ECSA; Supplementary Fig. 5) and mass activity (Supplementary Fig. 6).

Grooves promote uniform ORR rate

While the experimental results demonstrate that grooved electrodes provide improved bulk O_2 and H^+ transport properties, some aspects of local transport behaviour cannot be easily determined from bulk

https://doi.org/10.1038/s41560-023-01263-2

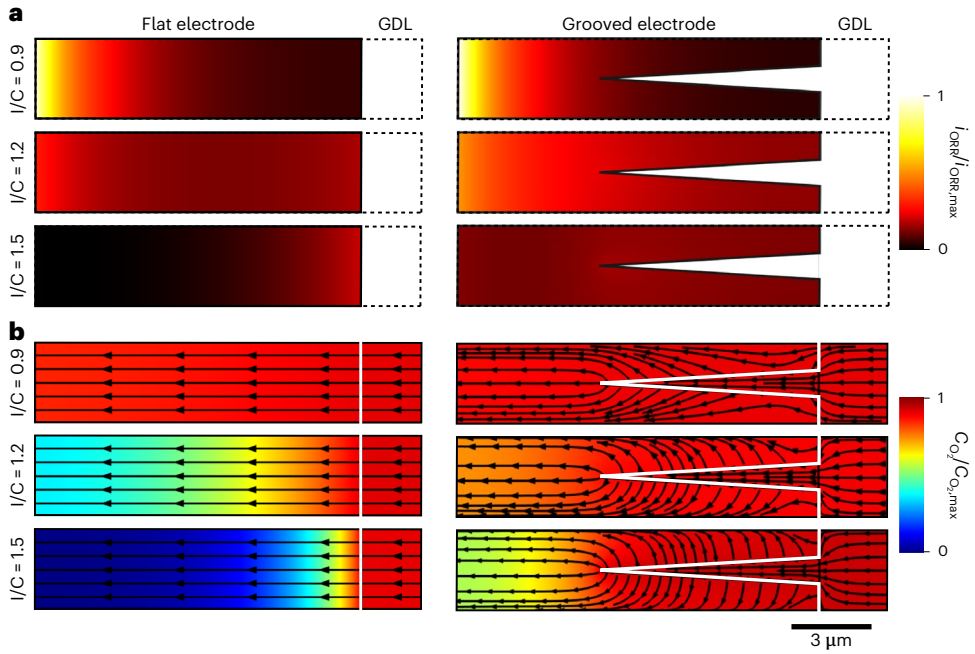

Fig. 4 | Local reaction rate and O_2 concentration in flat and grooved electrodes. a, **b**, Multiphysics modelling of flat and grooved electrodes (1 µm/3 µm): two-dimensional contour plots of the i_{ORR} at 0.7 V (**a**) and the O_2 concentration distribution ($C_{O_2}/C_{O_{2,max}}$) at 1.0 A cm^{-2} (**b**), with the arrows indicating the direction of O_2 diffusion.

measurements. Therefore, we used multiphysics modelling to estimate the local transport of reactants and products (O_2, H^+, e^- and H_2O) and predict the ORR rate (i_{ORR}) distribution throughout the electrode. At I/C = 0.9, the modelling results show that grooves have little effect on the i_{ORR} distribution, which is concentrated near the membrane interface due to the high H^+ transport resistance in the electrode, but they have a pronounced effect on i_{ORR} at I/C = 1.2 and 1.5 (Fig. 4a and Supplementary Fig. 7a). These results are consistent with the experimental observation of little performance enhancement at I/C = 0.9 with the incorporation of grooves, but large enhancement at higher I/C. The relatively uniform i_{ORR} throughout the grooved electrode at I/C = 1.2 and 1.5 confirms the enhancement in O_2 and H^+ transport. This interpretation is further supported by the more uniform concentration of O_2 throughout the grooved electrodes (Fig. 4b and Supplementary Fig. 7b) and the reduced Ohmic loss associated with H^+ transport (Supplementary Fig. 7c). While grooves provide significant performance benefits at both I/C= 1.2 and 1.5, the performance of the I/C = 1.5 grooved electrode remains relatively low, due to O_2 transport barriers associated with the local ionomer and agglomerate structure. As a result, the modelled i_{ORR} reaches its maximum average value for the I/C = 1.2 grooved electrode, in agreement with the experimental results.

Grooved electrodes facilitate effective O_2 and H^+ transport post carbon corrosion

The enhanced transport and increased performance provided by grooved electrodes at the beginning of test (BOT) became even more pronounced during durability testing. Following an accelerated stress test (AST) consisting of 500 cycles from 1.0 to 1.5 V in H_2/N_2 (ref. 47), the optimized grooved electrode (1 µm/3 µm, I/C = 1.2) provided notably higher end-of-test (EOT) performance compared with flat electrodes with I/C = 0.9 and 1.2 (Fig. 5a). The EOT grooved electrode current density at 0.7 V was 44% and 170% higher than that of the I/C = 0.9 and 1.2 EOT flat electrodes, respectively. Carbon corrosion leads to electrode compaction and decreased porosity[46], which increases the R_{O_2} and causes severe performance loss in flat electrodes. While all three EOT electrodes showed similar carbon loss (Fig. 5b), mass activity, ECSA and high-frequency resistance (HFR; Supplementary Table 4), they showed considerable differences in R_{O_2} (Fig. 5c) and ρ_{sheet} (Fig. 5d). Specifically, the EOT pressure-dependent and -independent R_{O_2} values for the grooved electrode were 12% and 38% lower, respectively, than those of the flat I/C = 0.9 electrode at EOT. SEM and HAADF-STEM images also confirmed that the grooves remained after degradation (Supplementary Fig. 8). Additionally, the ρ_{sheet} of the grooved electrode at 100% RH was 57% lower than that of the flat I/C = 0.9 electrode. Overall, the role of electrode grooves in facilitating effective O_2 transport while providing enhanced H^+ transport becomes even more important in degraded electrodes with collapsed pore structure, because these electrodes suffer from severe O_2 transport limitations in the absence of grooves.

Machine learning suggests path forwards

Electrochemical testing and multiphysics modelling have demonstrated the benefits of grooved electrodes for PEMFC performance and durability. However, the wide design space of the grooved electrode structure was not examined completely, due to limitations in experimental throughput and the computational load of multiphysics modelling. To accelerate the discovery of next-generation grooved electrode structures, we employed adaptive machine learning (ML) integrated directly with the multiphysics simulations to examine how tuning the groove depth (h) and width of the groove opening (d_1) may further improve PEMFC performance (Fig. 6).

The ML study revealed significant opportunities for improvement, with wider and deeper grooves expected to increase the performance by up to 60% compared with the baseline electrode (flat I/C = 0.9), and by up to 36% compared with the grooved electrode (I/C = 1.2). Although these predictions provide strong motivation to fabricate and test the identified optimum groove structures, a few realistic design challenges must be carefully considered. Firstly, the 1 µm/3 µm grooved electrode structure is already pushing the limits of our template-based fabrication method, so improved fabrication procedures would be needed to realize the predicted performance benefits of wider and deeper grooves. Secondly, the mechanical stability of grooved electrodes is

https://doi.org/10.1038/s41560-023-01263-2

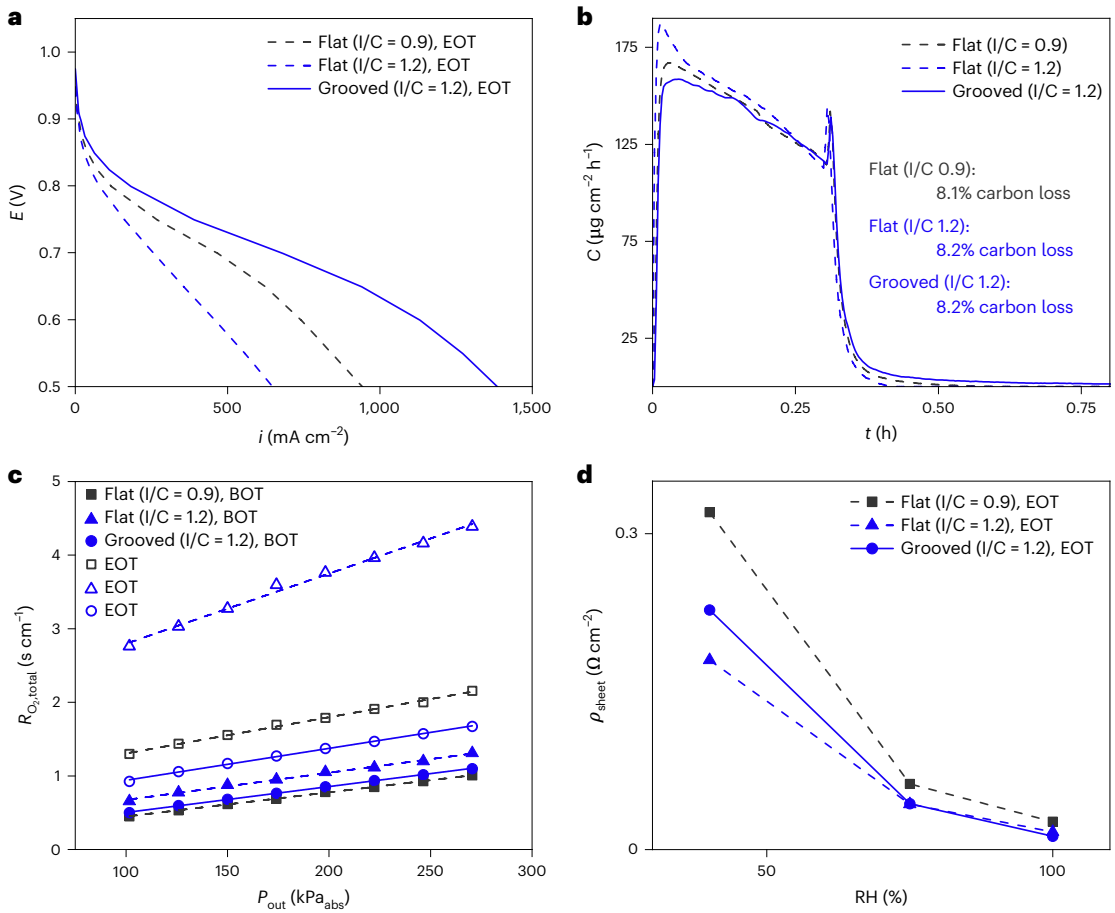

Fig. 5 | Durability of flat and grooved (1 µm/3 µm) electrodes. **a**–**d**, Comparison of performance of flat and grooved electrodes after 500 catalyst support AST cycles: polarization curves in H_2/air at 100% RH, 150 kPa_{abs} and 80 °C (**a**), carbon loss (*C*) during ASTs, measured using a non-dispersive infrared sensor (**b**), O_2 transport resistance measured at 60% RH (**c**) and sheet resistance measurements (**d**). The equivalent circuit models are shown in Supplementary Fig. 9, parameters are shown in Supplementary Table 5 and linear regression results are shown in Supplementary Table 6.

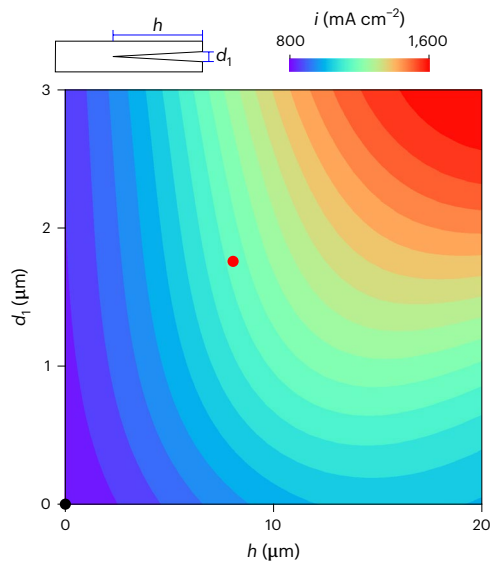

Fig. 6 | Future direction of grooved electrodes. Adaptive ML predictions of *i* at 0.7 V and 75% RH for a grooved electrode with I/C = 1.2, a groove period of 3 µm and 0.3 mg_{Pt} cm^{-2} cathode loading. The black and red circles represent the experimentally measured performance of the flat and grooved electrodes, respectively. The parameters *h* and d_1 of the grooved electrode are defined schematically at the top of the figure.

expected to decrease as the electrode ridge aspect ratio increases, making the ridges more prone to fracture and collapse. A systematic study is required to understand the effect of cell compression force on the integrity of the grooved electrode structure. Despite the challenges, aiming towards higher aspect ratio electrode ridges while carefully considering these factors presents a promising pathway to further enhance grooved electrode performance.

Conclusion

We have reported here an alternative PEMFC electrode structure, the grooved electrode, that provides significant performance and durability benefits. The grooved electrode consists of catalyst ridges with high ionomer content separated by empty grooves, which provide effective pathways for the transport of H^+ and O_2, respectively. Compared with an optimized flat baseline electrode, the grooved electrode provides a 60% decrease in H^+ transport resistance at 100% RH, without significant change in O_2 transport resistance. Multiphysics modelling of the transport of reactants and products and ORR reaction revealed that grooved electrodes exhibit a relatively uniform ORR rate throughout the electrode, enabling improved catalyst performance and reduced transport losses compared with a flat baseline electrode. The benefits of the grooved architecture are even more apparent in degraded electrodes with collapsed pore structure, in which the grooves play a critical role in facilitating O_2 transport through the electrode. While this work has already demonstrated significant advances in PEMFC performance using grooved electrodes, adaptive ML examination of

a wide design space revealed ample opportunities for further performance improvements. Therefore, further work is needed to continue to advance the frontiers of high power density PEMFCs using optimized grooved electrode architectures.

Methods

Template fabrication

We fabricated silicon-based templates at the Center for Integrated Nanotechnologies, a joint facility of Los Alamos National Laboratory and Sandia National Laboratories. Silicon wafers with a 10.16 cm diameter were first baked at 150 °C for 3 min and then spin-coated with (1) hexamethyldisilazane at 4,000 rpm and (2) a positive photoresist (AZ5214E, MicroChemicals) at 1,500 rpm. After spin-coating, the wafers were soft-baked at 110 °C for 1.5 min. We used a maskless UV aligner system (MLA 150, Heidelberg Instruments) to expose a grooved pattern onto the photoresist at 220 mJ cm^{-2}. After the UV exposure step, we removed the non-cross-linked portion of the photoresist by soaking for 1 min in a developer solution (AZ 300 MIF, AZ Electronic Materials). The wafer was rinsed with deionized water after development. Then we loaded the wafer with patterned photoresist onto a deep reactive ion etching reactor (730 SLR, Plasma-Therm). Rather than using the conventional Bosch method based on a time-multiplexed process that alternates SF_6 and C_4F_8 (for plasma etching and deposition of a passivation layer, respectively), we used a SF_6–C_4F_8 mixed process to create the desired wall profiles (Supplementary Fig. 10). The templates were etched to depths of 10–13 µm, depending on the density of the grooves. After etching, the photoresists were completely removed in piranha solution and then thoroughly rinsed with deionized water. Piranha solution was also used to hydroxylate the surface to render the silicon surface hydrophilic, to aid catalyst ink penetration into the silicon template. A photograph of a completed silicon template is shown in Supplementary Fig. 11. The wafer was cleaved using a diamond scribe to produce smaller pieces for the fabrication of 5-cm^2 electrodes.

Electrode fabrication

A schematic of the electrode fabrication procedure is shown in Supplementary Fig. 12. The catalyst ink was prepared by mixing the catalyst (TEC10E40E, Tanaka Precious Metals), ionomer dispersion (D2020, Chemours) and isopropanol–water (12:1, v/v) in a glass vial. The I/C ratio of the electrode was controlled by varying the content of ionomer dispersion. The ink was stirred for 20 min, then bath-sonicated for 20 min before coating. The ink was coated onto the patterned templates using a wire-wound rod on a hot plate heated to 80 °C. The resulting Pt loading was 0.3 mg_{Pt} cm^{-2}, with less than 5% variation, determined through spot X-ray fluorescence (XRF) measurements (Quant'X EDXRF, Thermo Fisher). The anode was fabricated by ultrasonic spraying (ExactaCoat, Sono-Tek) a catalyst ink prepared with a lower-Pt-content catalyst (TEC10V20E), ionomer dispersion and *n*-propanol–water (4:3, v/v) onto a membrane (NR-211, Chemours).

To calibrate the XRF measurements, we performed a three-point calibration using high-precision calibration standards (Micromatter Technologies). However, in principle, both electrode grooves and different I/C could cause deviation from this calibration, because of a larger amount of material that could attenuate both primary and secondary X-rays. In particular, the grooved architecture leads to a modest increase in electrode thickness (~25%) compared with the flat electrode, which could cause deviation from the calibration. To test this hypothesis, we prepared Pt/C catalysts mixed with Ketjen black and ionomer, and coated several layers of the ink onto a substrate by automated ultrasonic spray, measuring the thickness (via a micrometer) and Pt loading (via XRF) after every 20 coatings. The results of these measurements are summarized in Supplementary Table 7. We observed that the Pt loading measured via XRF increased linearly with electrode thickness, up to 158 µm, as shown in Supplementary Fig. 13. As the linear relationship between measured loading and thickness was maintained at least up to 158 µm, it is safe to conclude that the ~15 µm electrodes used in our study did not deviate from the three-point calibration.

The ink was stirred for 20 min and then bath-sonicated for 20 min before spraying. The anodic Pt loading was 0.1 mg_{Pt} cm^{-2} with I/C = 0.5. After coating the electrode, the electrode/template was hot-pressed onto the membrane on which the anode electrode was coated under a pressure of 135 kg cm^{-2} at 130 °C for 5 min. The membrane electrode assembly (MEA)/template was subsequently immersed in 1 M NaOH for 12 h at room temperature to dissolve the silicon template, but the template was released before complete dissolution of the silicon, which was attributed to the silicon ridge structure dissolving first. MEA immersion in NaOH is a common technique used to enhance decal methods in fuel cells[26]. The patterned silicon templates used in this work could not be reused, because they had dissolved in NaOH solution. Further studies are needed to develop reusable templates that can be released from the electrode without dissolution. The MEA was rinsed in deionized water for 1 h, then reprotonated in 0.5 M H_2SO_4 heated to 70 °C for 2 h and finally rinsed again in deionized water for 1 h. Example SEM images of the fabricated templates and electrodes are shown in Supplementary Fig. 1.

Electrode characterization

Thin cross-sections of the grooved electrodes were prepared for STEM analysis by embedding the individual MEAs in epoxy. The epoxy kit used for embedding the ultramicrotomed samples included a mixture of Araldite 6005, dodecenylsuccinic anhydride and benzyldimethylamine. Embedding moulds were half-filled with epoxy, which was cured ahead of time to prevent the sample from sinking to the bottom of the epoxy block. Sections of air-dried MEA (approximately 2 mm × 4 mm in size) were placed on the half-filled, previously cured blocks and then the embedding moulds were filled to the top and cured in an oven at 60 °C for 24 h. The embedded samples were then processed by rough trimming the epoxy block and subsequent slicing by diamond knife ultramicrotomy.

The nominally 75-nm-thick slices were imaged with a JEOL NEOARM microscope operated at 80 kV and equipped with dual solid-state detectors for EDS analysis. Elemental maps were acquired using the JEOL Analysis Station software with a beam current of ~750 pA and a field of view of 9.8 µm × 9.8 µm (512 × 512 pixels). These elemental maps were processed by averaging four neighbouring pixels and applying a Gaussian filter, resulting in a map with 19.2 nm pixel resolution (256 × 256 pixels). The electrodes were also imaged using an UltraXRM-L200 nanoscale X-ray tomography instrument (Carl Zeiss X-ray Microscopy). The samples were cut into small pieces and mounted on a vertical transmission electron microscopy (TEM) grid clamp. Specifically, an ~2-mm-wide slice was prepared by cutting through the sample with a fresh razor blade against a cutting board. The sample was then mounted onto a flat-backed clip (345360-0000-123, Zeiss). One end of the slice was held by the clip and the other end was held in place by a 2-mm-diameter magnet. At 0°, the X-ray beam orientation was perpendicular to the thickness of the sample. This mounting method kept the sample stationary and unable to flex with time. Additionally, a gold microbead (3 µm diameter) was placed on the back surface of the substrate for use as a fiducial in the radiographic image alignment. The TEM grid clamp limited the rotation of the sample to approximately 125°, instead of the nominal 180°. The radiographs were aligned and reconstructed. The reconstructed slices were rendered using the Avizo software (FEI).

Fuel cell assembly and testing

All fuel cells were tested using a commercial fuel cell test station (850 Fuel Cell Test Station, Scribner Associates) with differential cell hardware (as reported by ref. 44) with a 215-µm-thick GDL (SGL 22BB, SGL Carbon) used for both the anode and cathode and polyurethane gaskets (Poron, Rogers). Electrochemical analyses included measurements of

mass activity, polarization curves, ECSA, sheet resistance, EIS and O_2 transport resistance. For the mass activity measurements, a constant potential of 0.9 V (HFR-corrected) with H_2/O_2 (1,000/3,000 standard cubic centimeters per minute (sccm)) was held for 15 min. For the polarization curves, constant potentials from 0.40 V to the open circuit voltage with H_2/air (1,000/3,000 sccm) were held for 4 min each, and the HFR was recorded simultaneously at 5 kHz (Supplementary Fig. 14). For the ECSA measurements, a potential sweep from 0.08 to 0.98 V at a rate of 50 mV s^{-1} at 35 °C was conducted with H_2 on the anode (1,000 sccm) and ~500% RH. The cathode was purged with N_2 before measurement and the cathode flow was set to zero during the measurement. For each measurement, the potential was cycled seven times, the double layer current was determined on the basis of the average current between 0.4 and 0.45 V, and this double layer current was subtracted from the measured current before calculating the area under the curve between 0.1 and 0.4 V. We divided the current density by the sweep rate and integrated between 0.1 and 0.4 V to determine the hydrogen underpotential deposition (HUPD) charge, and then calculated the surface area based on a charge of 210 μC cm^{-2} for formation of an HUPD monolayer. We normalized this surface area by the Pt loading measured via XRF to determine the ECSA. Cyclic voltammograms are shown in Supplementary Fig. 15. For the sheet resistance measurements, we applied a 10 mV perturbation at 0.5 V and the frequency was swept from 40 kHz to 0.5 Hz with H_2/N_2 (1,000/3,000 sccm). We fitted an equivalent circuit model to extract the sheet resistance (Supplementary Figs. 3 and 9). The fitted parameters are shown in Supplementary Tables 1 and 5. For the EIS measurements during cell polarization, we applied a 10% d.c. perturbation at 2.0 A cm^{-2} and a frequency sweep from 10 kHz to 0.1 Hz with 1,000/3,000 sccm of H_2/air and H_2/helox. We fitted an equivalent circuit model to extract the mass transport resistance (Supplementary Table 2). The fitted parameters are shown in Supplementary Table 2. Limiting current measurements of O_2 transport resistance were conducted by measuring the current density from 0.4 to 0.1 V (16 s hold for each potential step) while flowing H_2/0.5% O_2 (500/5,000 sccm) at eight different absolute pressures (100–275 kPa_{abs}) at 60% RH. The fitted parameters are shown in Supplementary Tables 3 and 6. Unless otherwise stated, all tests were performed at 100% RH, 80 °C and 150 kPa_{abs}.

We performed carbon corrosion AST experiments according to the protocol published in the USDRIVE Fuel Cell Technical Team Roadmap[47]. Specifically, the cell was operated with a triangle sweep cycle (cycled 500 times) from 1.0 to 1.5 V at a rate of 500 mV s^{-1} with H_2/N_2 (200/200 sccm) under atmospheric pressure at 100% RH and 80 °C. We measured the concentration of CO_2 released during the AST using a non-dispersive infrared detector (Model 600-NDIR, California Analytical Instruments) connected to the cathode outlet. The changes in mass activity, ECSA and HFR after AST are summarized in Supplementary Table 4.

Multiphysics modelling and finite element method simulations

Finite element method simulations of the grooved electrodes were implemented in COMSOL Multiphysics. Our state-of-the-art model follows the general approach of ref. 25 and integrates electrochemistry, fluid dynamics (describing liquid, vapour and ionomer-dissolved water transport as well as oxygen and hydrogen transport), heat transfer and charge transport in the GDL, microporous layer (MPL), cathode and anode electrodes, and ionomer membrane. Simulations were initially performed on baseline flat electrodes and benchmarked against experimental polarization curves for model development and validation before being extended to the grooved electrode architecture. Due to the high computational demand and translational invariance of the grooves, we considered only two-dimensional simulations of the groove electrode cross-section and truncated the simulation domain to a unit cell comprising one groove subject to periodic boundary conditions (Supplementary Fig. 16). The morphological and transport parameters for all domains were either measured experimentally or extracted from manufacturer datasheets. The values of some reaction kinetic parameters (for example, the ORR exchange current density and structural features of agglomerates) and transport properties (for example, gas and proton transport tortuosity) were adjusted to ensure that the model matches the experimentally measured current densities for the baseline electrodes. Identical parameter values were used for the flat and grooved electrodes. Transport within the grooves was modelled following the approach of ref. 48 for modelling transport in electrode voids, with mass conservation of the gas and liquid phases approximated by the same transport equations as used in the GDL and MPL, with a critical pore radius of a few tens of micrometres. The groove domains were considered a porous medium with the volume fraction of the pore phase equal to 1 and the solid phase equal to 0. The developed approach is well justified by the excellent agreement between experimental and simulation results for various grooved electrodes (Supplementary Fig. 17). For further details on the model, see Supplementary Note 1. The datasets are provided in Supplementary Data 1.

Adaptive machine learning

A representation of the adaptive learning framework developed to optimize the grooved electrode architecture is shown in Supplementary Fig. 16b. The adaptive learning strategy integrated four steps that guide the next set of multiphysics calculations to be performed while minimizing the need for computationally demanding and time-consuming finite element method simulations. The first step was the generation of a training database with various grooved electrode structures identified by a set of input descriptors and output properties. We considered trapezoidal groove channel geometries indexed through four structural parameters: the unit cell period w, the groove penetration depth h, the groove opening size d_1 at the MPL interface and the groove base size d_2 within the electrode (Supplementary Fig. 16a). The constraints $d_1 < w$ and $d_2 < d_1$, which must be satisfied for the electrode structure to be physically possible, were enforced by parameterizing d_1 and d_2 in terms of the dimensionless variables $l_1 = d_1/w$ and $l_2 = 1 - (d_2/d_1)$, where l_1 is the dimensionless length of the groove opening and l_2 is a dimensionless representation of the groove shape. The current density i at cell voltage (V_{cell}) = 0.7 V and RH = 75% was considered as the output property of interest, with I/C maintained constant at 1.2. Fifty multiphysics numerical simulations of randomly selected grooved electrode geometries were performed to create the initial training database, with the input parameters in the following ranges: 0.5 μm < w < 40 μm, 0.05 μm < h < 20 μm, 0.05 < l_1 < 0.95 and 0.05 < l_2 < 0.95. In the second step of the learning loop, this database was used to train an artificial neural network (ANN) regression model, implemented in Python via the scikit-learn package[49]. We split the initial data into an 80-to-20 training-to-cross-validation size ratio and used the new electrode architectures simulated following the adaptive learning framework suggestions as testing sets. We optimized the ANN algorithm hyperparameters via a comprehensive grid search using 20 random shuffle splits of the training data while targeting the minimization of the root mean squared error (r.m.s.e) cost function. The final ANN architecture involved three hidden layers with 64 neurons each using a hyperbolic tangent activation function, an adaptive learning rate and a ridge regression regularization parameter fixed at 0.05. Uncertainty quantification was implemented by training the optimized ANN algorithm in 1,000 bootstraps (synthetic 'copies' of the original dataset, generated via a random selection of samples with replacement) and using all the model's predictions to compute the average μ and standard deviation σ of the current density for any grooved electrode design[50]. This approach reduces the possibility of overfitting. In the third step of the adaptive learning loop, a computational design tool was developed by combining the ML model and uncertainty quantification with global optimization methods[51]. This tool enables a search in

the space of unexplored grooved electrode architectures and chooses the best samples (those that either maximize the current density or would decrease model uncertainty) to be considered in the next round of multiphysics calculations by maximizing the expected improvement (EI) acquisition function, $\mathrm{EI}(\{x_i\}) = \sigma(\{x_i\}) \times [\varphi(z) + z\Phi(z)]$. Here, $\varphi(z)$ is the normal density probability function and $\Phi(z)$ is the corresponding cumulative distribution function. Also, $z = \frac{\mu(\{x_i\}) - \mu(\{x_i^*\})}{\sigma(\{x_i\})}$, where $\mu(\{x_i\})$ and $\sigma(\{x_i\})$ are the average current density and its standard deviation, respectively, for a set of grooved electrode input parameters $\{x_i\} = \{w, h, l_1, l_2\}$, and $\{x_i^*\}$ represents the grooved electrode architecture with the highest current density known so far. In the fourth step of the adaptive learning design, ten new samples were selected for simulation, with calculation of the r.m.s.e, the mean absolute percentage error (MAPE) and coefficient of determination (R^2) after each loop iteration. We iterated through the adaptive learning loop 30 times (10 new geometries per iteration) for a total of 350 data points (50 initial + 300 from adaptive learning). The final ANN model shows r.m.s.e. = 13.6 ± 3.6 mA cm^{-2}, MAPE = 0.6 ± 0.1% and R^2 =0.993 ± 0.003 (to be compared with r.m.s.e. = 43.5 ± 11.5 mA cm^{-2}, MAPE = 2.3 ± 1.0% and R^2 = 0.963 ± 0.015 in the first iteration). This model was used to generate the plot in Fig. 6. The training and adaptive learning datasets are provided in Supplementary Data 1.

Data availability

The authors declare that the data supporting the findings of this study are available within the paper and its Supplementary Information. Source data are provided with this paper.

References

1. Li, J. & Thompson, D. W. J. Widespread changes in surface temperature persistence under climate change. *Nature* **599**, 425–430 (2021).
2. Jewell, J. et al. Limited emission reductions from fuel-subsidy removal except in energy-exporting regions. *Nature* **554**, 229–233 (2018).
3. Jiao, K. et al. Designing the next generation of proton-exchange membrane fuel cells. *Nature* **595**, 361–369 (2021).
4. Cullen, D. A. et al. New roads and challenges for fuel cells in heavy-duty transportation. *Nat. Energy* **6**, 462–474 (2021).
5. Forner-Cuenca, A. et al. Engineered water highways in fuel cells: radiation grafting of gas diffusion layers. *Adv. Mater.* **27**, 6317–6322 (2015).
6. Khedekar, K. et al. Probing heterogeneous degradation of catalyst in PEM fuel cells under realistic automotive conditions with multi-modal techniques. *Adv. Energy Mater.* **11**, 2101794 (2021).
7. Topalov, A. A. et al. Dissolution of platinum: limits for the deployment of electrochemical energy conversion? *Angew. Chem. Int. Ed.* **51**, 12613–12615 (2012).
8. Banas, C. J., Uddin, M. A., Park, J., Bonville, L. J. & Pasaogullari, U. Thinning of cathode catalyst layer in polymer electrolyte fuel cells due to foreign cation contamination. *J. Electrochem. Soc.* **165**, F3015 (2018).
9. Kodama, K., Nagai, T., Kuwaki, A., Jinnouchi, R. & Morimoto, Y. Challenges in applying highly active Pt-based nanostructured catalysts for oxygen reduction reactions to fuel cell vehicles. *Nat. Nanotechnol.* **16**, 140–147 (2021).
10. Papageorgopoulos, D. Fuel cell technologies overview. In *2021 Annual Merit Review and Peer Evaluation Meeting* (US Department of Energy Hydrogen and Fuel Cell Technologies Office, 2021).
11. Wang, X. X. et al. Ordered Pt_3Co intermetallic nanoparticles derived from metal–organic frameworks for oxygen reduction. *Nano Lett.* **18**, 4163–4171 (2018).
12. Chen, C. et al. Highly crystalline multimetallic nanoframes with three-dimensional electrocatalytic surfaces. *Science* **343**, 1339–1343 (2014).
13. Strasser, P. et al. Lattice-strain control of the activity in dealloyed core–shell fuel cell catalysts. *Nat. Chem.* **2**, 454–460 (2010).
14. Qiao, Z. et al. 3D porous graphitic nanocarbon for enhancing the performance and durability of Pt catalysts: a balance between graphitization and hierarchical porosity. *Energy Environ. Sci.* **12**, 2830–2841 (2019).
15. Cui, C., Gan, L., Heggen, M., Rudi, S. & Strasser, P. Compositional segregation in shaped Pt alloy nanoparticles and their structural behaviour during electrocatalysis. *Nat. Mater.* **12**, 765–771 (2013).
16. Li, J. et al. Hard-magnet $L1_0$–CoPt nanoparticles advance fuel cell catalysis. *Joule* **3**, 124–135 (2019).
17. Chen, W. et al. Neighboring Pt atom sites in an ultrathin FePt nanosheet for the efficient and highly CO-tolerant oxygen reduction reaction. *Nano Lett.* **18**, 5905–5912 (2018).
18. Chen, J., Lim, B., Lee, E. P. & Xia, Y. Shape-controlled synthesis of platinum nanocrystals for catalytic and electrocatalytic applications. *Nano Today* **4**, 81–95 (2009).
19. Zhao, X. et al. Octahedral $Pd@Pt_{1.8}Ni$ core–shell nanocrystals with ultrathin PtNi alloy shells as active catalysts for oxygen reduction reaction. *J. Am. Chem. Soc.* **137**, 2804–2807 (2015).
20. Higgins, D. C., Meza, D. & Chen, Z. Nitrogen-doped carbon nanotubes as platinum catalyst supports for oxygen reduction reaction in proton exchange membrane fuel cells. *J. Phys. Chem. C* **114**, 21982–21988 (2010).
21. Mauger, S. A. et al. Development of high-performance roll-to-roll-coated gas-diffusion-electrode-based fuel cells. *J. Power Sources* **506**, 230039 (2021).
22. Jhong, H.-R., Brushett, F. R. & Kenis, P. J. A. The effects of catalyst layer deposition methodology on electrode performance. *Adv. Energy Mater.* **3**, 589–599 (2013).
23. Breitwieser, M. et al. Tailoring the membrane-electrode interface in PEM fuel cells: a review and perspective on novel engineering approaches. *Adv. Energy Mater.* **8**, 1701257 (2018).
24. Jinnouchi, R. et al. The role of oxygen-permeable ionomer for polymer electrolyte fuel cells. *Nat. Commun.* **12**, 4956 (2021).
25. Weber, A. Z. et al. A critical review of modeling transport phenomena in polymer-electrolyte fuel cells. *J. Electrochem. Soc.* **161**, F1254 (2014).
26. Wilson, M. S. & Gottesfeld, S. High performance catalyzed membranes of ultra-low Pt loadings for polymer electrolyte fuel cells. *J. Electrochem. Soc.* **139**, L28–L30 (1992).
27. Wang, W. et al. Tuning nanowires and nanotubes for efficient fuel-cell electrocatalysis. *Adv. Mater.* **28**, 10117–10141 (2016).
28. Breitwieser, M., Klingele, M., Vierrath, S., Zengerle, R. & Thiele, S. Tailoring the membrane–electrode interface in PEM fuel cells: a review and perspective on novel engineering approaches. *Adv. Energy Mater.* https://doi.org/10.1002/aenm.201701257 (2018).
29. Shukla, S., Domican, K., Karan, K., Bhattacharjee, S. & Secanell, M. Analysis of low platinum loading thin polymer electrolyte fuel cell electrodes prepared by inkjet printing. *Electrochim. Acta* **156**, 289–300 (2014).
30. Yang, G. et al. Building electron/proton nanohighways for full utilization of water splitting catalysts. *Adv. Energy Mater.* **10**, 1903871 (2020).
31. Paul, M. T. Y., Kim, D., Saha, M. S., Stumper, J. & Gates, B. D. Patterning catalyst layers with microscale features by soft lithography techniques for proton exchange membrane fuel cells. *ACS Appl. Energy Mater.* https://doi.org/10.1021/acsaem.9b01754 (2020).
32. Koh, J. K. et al. A facile preparation method of surface patterned polymer electrolyte membranes for fuel cell applications. *J. Mater. Chem. A* **2**, 8652–8659 (2014).

33. Zhang, L., Porter, T., Guillory, S., Chi, C. & Arges, C. G. Patterning polymer electrolyte membrane for fuel cell and electrolysis applications. *ECS Trans.* **77**, 1325 (2017).
34. Debe, M. K. Tutorial on the fundamental characteristics and practical properties of nanostructured thin film (NSTF) catalysts. *J. Electrochem. Soc.* **160**, F522–F534 (2013).
35. Liu, Y. et al. Determination of electrode sheet resistance in cathode catalyst layer by AC impedance. *ECS Trans.* **11**, 473 (2007).
36. Salari, S., Stumper, J. & Bahrami, M. Direct measurement and modeling relative gas diffusivity of PEMFC catalyst layers: the effect of ionomer to carbon ratio, operating temperature, porosity, and pore size distribution. *Int. J. Hydrogen Energy* **43**, 16704–16718 (2018).
37. Zhang, H. et al. A cathode-supported solid oxide fuel cell prepared by the phase-inversion tape casting and impregnating method. *Int. J. Hydrogen Energy* **47**, 18810–18819 (2022).
38. Shi, N. et al. Performance and DRT analysis of P-SOFCs fabricated using new phase inversion combined tape casting technology. *J. Mater. Chem. A* **5**, 19664–19671 (2017).
39. Yu, Z., Carter, R. N. & Zhang, J. Measurements of pore size distribution, porosity, effective oxygen diffusivity, and tortuosity of PEM fuel cell electrodes. *Fuel Cells* **12**, 557–565 (2012).
40. He, W., Lv, W. & Dickerson, J. *Gas Transport in Solid Oxide Fuel Cells* (Springer, 2014).
41. Kobayashi, A. et al. Effect of Pt and ionomer distribution on polymer electrolyte fuel cell performance and durability. *ACS Appl. Energy Mater.* **4**, 2307–2317 (2021).
42. Orfanidi, A. et al. The key to high-performance low-Pt-loaded electrodes. *J. Electrochem. Soc.* **164**, F418–F426 (2017).
43. Makharia, R., Mathias, M. F. & Baker, D. R. Measurement of catalyst layer electrolyte resistance in PEFCs using electrochemical impedance spectroscopy. *J. Electrochem. Soc.* **152**, A970 (2005).
44. Baker, D. R., Caulk, D. A., Neyerlin, K. C. & Murphy, M. W. Measurement of oxygen transport resistance in PEM fuel cells by limiting current methods. *J. Electrochem. Soc.* **156**, B991 (2009).
45. Arisetty, S. et al. Catalyst durability in PEM fuel cells with low platinum loading. *J. Electrochem. Soc.* **159**, B455–B462 (2012).
46. Macauley, N. et al. Carbon corrosion in PEM fuel cells and the development of accelerated stress tests. *J. Electrochem. Soc.* **165**, F3148–F3160 (2018).
47. Benjamin, T. et al. *Fuel Cell Technical Team Roadmap* (USDRIVE, 2017); https://www.energy.gov/sites/prod/files/2017/11/f46/FCTT_Roadmap_Nov_2017_FINAL.pdf
48. Zenyuk, I. V., Taspinar, R., Kalidindi, A. R., Kumbur, E. C. & Litster, S. Computational and experimental analysis of water transport at component interfaces in polymer electrolyte fuel cells. *J. Electrochem. Soc.* **161**, F3091–F3103 (2014).
49. Pedregosa, F. et al. Scikit-learn: machine learning in Python. *J. Mach. Learn. Res.* **12**, 2825–2830 (2011).
50. Hastie, T., Tibshirani, R. & Friedman, J. *The Elements of Statistical Learning: Data Mining, Inference, and Prediction* 2nd edn (Springer, 2009).
51. Jones, D. R., Schonlau, M. & Welch, W. J. Efficient global optimization of expensive black-box functions. *J. Glob. Optim.* **13**, 455–492 (1998).

Acknowledgements

C.L., H.Y., D.A.C., T.A.A., S.K.B., R.M., R.L.B. and J.S.S. gratefully acknowledge support from the Hydrogen and Fuel Cell Technologies Office, Office of Energy Efficiency and Renewable Energy, US Department of Energy through the Million Mile Fuel Cell Truck (M2FCT) consortium, technology managers G. Kleen and D. Papageorgopoulos. C.L., W.J.M.K.-K., B.M.P., T.A.A., S.K.B., R.L.B. and J.S.S. gratefully acknowledge support from the Laboratory Directed Research and Development programme at Los Alamos National Laboratory (projects 20202000DR and 20210915PRD2). This work was performed, in part, at the Center for Integrated Nanotechnologies, an Office of Science User Facility operated for the US Department of Energy Office of Science by Los Alamos National Laboratory (contract 89233218CNA000001) and Sandia National Laboratories (contract DE-NA-0003525). C.L. acknowledges support from the Natural Sciences and Engineering Research Council of Canada. We also thank Y. Muniz and A. Rahman for valuable discussions on multiphysics simulations and the ML methods, respectively, used in this work. Electron microscopy was conducted as part of a user project at the Center for Nanophase Materials Sciences, which is a US Department of Energy, Office of Science User Facility at Oak Ridge National Laboratory.

Author contributions

C.L., S.K.B., R.M., R.L.B. and J.S.S. developed the intellectual concept and designed the experiments. W.J.M.K.-K. performed multiphysics modelling and machine learning. H.Y. and D.A.C. performed HAADF-STEM and image analyses. B.M.P. performed nanoscale X-ray computed tomography. C.L. performed the electrochemical experiments. T.A.A. performed XRF calibration and analysis. C.L. and J.S.S. analysed the experimental data. C.L., W.J.M.K.-K. and J.S.S. wrote the paper.

Competing interests

The authors declare no competing interests.

Additional information

Supplementary information The online version contains supplementary material available at https://doi.org/10.1038/s41560-023-01263-2.

Correspondence and requests for materials should be addressed to Jacob S. Spendelow.

Peer review information *Nature Energy* thanks Meng Ni and the other, anonymous, reviewer(s) for their contribution to the peer review of this work.